



HAL
open science

C II*/C II ratio in high-redshift DLAs: ISM phase separation drives the observed bimodality of [C II] cooling rates

S. A. Balashev, K. N. Telikova, P. Noterdaeme

► **To cite this version:**

S. A. Balashev, K. N. Telikova, P. Noterdaeme. C II*/C II ratio in high-redshift DLAs: ISM phase separation drives the observed bimodality of [C II] cooling rates. Monthly Notices of the Royal Astronomical Society: Letters, 2022, 509, pp.L26-L30. 10.1093/mnrasl/slab119 . insu-03748299

HAL Id: insu-03748299

<https://insu.hal.science/insu-03748299>

Submitted on 6 Jul 2023

HAL is a multi-disciplinary open access archive for the deposit and dissemination of scientific research documents, whether they are published or not. The documents may come from teaching and research institutions in France or abroad, or from public or private research centers.

L'archive ouverte pluridisciplinaire **HAL**, est destinée au dépôt et à la diffusion de documents scientifiques de niveau recherche, publiés ou non, émanant des établissements d'enseignement et de recherche français ou étrangers, des laboratoires publics ou privés.

C II*/C II ratio in high-redshift DLAs: ISM phase separation drives the observed bimodality of [C II] cooling rates

S. A. Balashev¹ , ¹★ K. N. Telikova¹  and P. Noterdaeme²

¹*Ioffe Institute, Politekhnicheskaya 26, 194021 Saint Petersburg, Russia*

²*Institut d'Astrophysique de Paris, CNRS-SU, UMR 7095, 98bis bd Arago, 75014 Paris, France*

Accepted 2021 October 25. Received 2021 October 19; in original form 2021 August 13

ABSTRACT

We discuss observations of C II*/C II ratios and cooling rates due to [C II] 158 μm emission in high-redshift intervening damped Lyman- α (DLA) systems towards quasars. We show that the observed bimodality in the C II cooling rates actually reflects a bimodality in the C II*/C II–metallicity plane that can be naturally explained by phase segregation of the neutral medium, without invoking differences in star-formation scenarios. Assuming realistic distributions of the physical parameters to calculate the phase diagrams, we also reproduce qualitatively the metallicity dependence of this bimodality. We emphasize that high- z DLAs mostly probe low-metallicity gas ($Z \lesssim 0.1 Z_{\odot}$), where heating is dominated by cosmic rays (and/or turbulence), and not by photoelectric heating. Therefore, even if the gas of DLA is predominantly cold (where the cooling is dominated by [C II]), the excitation of C II can be used to derive the cosmic ray ionization rate (and/or turbulent heating), but not the UV field, as was previously considered. Alternatively, if the gas in DLA is predominantly warm, C II*/C II can be used to constrain its number density. Finally, we also discuss the importance of the ionized medium, which, if also present along the line of sight, can significantly increase the average C II*/C II ratio.

Key words: galaxies: high-redshift – galaxies: ISM – quasars: absorption lines.

1 INTRODUCTION

It is well established that for a wide range of physical conditions, the phase diagram of the neutral interstellar medium consists of two stable phases (Field, Goldsmith & Habing 1969; Wolfire et al. 1995): A cold (with characteristic temperature $T \lesssim 100$ K) and a warm ($T \lesssim 10^4$ K) phase. These phases coexist in pressure equilibrium within some range of thermal pressures, where the denser cold neutral medium (CNM) with small filling factor ($\lesssim 1$ per cent) is embedded into the more diffuse warm neutral medium (WNM). This two-phase model is a natural consequence of the thermal balance, where the cooling is dominated by line emission (Ly α , [C II] 158 μm and [O I] 63 μm) and heating is primary due to photoelectric effect and cosmic rays (Field et al. 1969). Since the photoelectric heating scales with UV flux, the phase diagram at solar metallicity depends on the star-formation rate (Wolfire et al. 2003). This motivated Wolfe, Prochaska & Gawiser (2003) to develop a method to constrain the star-formation rates in high-redshift Damped Lyman- α (DLA, Wolfe, Gawiser & Prochaska 2005) systems towards quasar (QSO) sightlines, assuming that the photoelectric heating equates the C II cooling rate, itself being estimated through measurements of C II* column densities (following Pottasch, Wesselius & van Duinen 1979). The obtained C II cooling rates present an evident bimodality (Wolfe et al. 2008), which was interpreted by the authors as arising from a bimodality in star-formation regimes in the galaxies associated with the DLAs.

However, the majority of DLAs probe WNM (Srianand et al. 2005; Kanekar et al. 2014), which is actually predominantly cooled by Ly α emission (see e.g. Liszt 2002; Draine 2011) and not by [C II] emission, which is the main coolant only in CNM. In particular, studies by Liszt (2002), Wolfe et al. (2003), Srianand et al. (2005), and Neeleman, Prochaska & Wolfe (2015) of the C II*/C II ratio in DLAs mentioned that C II* is less excited in WNM than in CNM due to difference in densities and temperatures. Even more, Srianand et al. 2005 have been already shown that since thermal pressures, at which WNM and CNM coexist, is metallicity-dependent, the typical C II*/C II ratio increase with metallicity decrease. Emission line studies also indicate that the [C II] 158 μm emission is indeed typically ~ 20 times weaker in the WNM than in the CNM (e.g. Pineda et al. 2013). Finally, observations and simulations show that ionized gas can also provide a large fraction (at least in our Galaxy) of C II observed in emission (e.g. Roy et al. 2017; Ramos Padilla et al. 2021).

In this letter, we discuss the C II excitation in the low metallicity gas that is typically associated with DLAs and revisit the origin of the bimodality in the distribution of the observed C II cooling rates.

2 C II FINE-STRUCTURE

The ground term of singly ionized carbon, C II ($1s^2 2s^2$) $2p^2 P^{\circ}$, splits into two fine-structure levels, $^2P_{1/2}^{\circ}$ (the ground one), and $^2P_{3/2}^{\circ}$ (usually denoted as C II*). The energy separation between these levels is 63.42 cm^{-1} (or 91.25 K), and the corresponding fine-structure [C II] $\lambda 158 \mu\text{m}$ transition from typically collisionally excited $^2P_{3/2}^{\circ}$ level (Goldsmith et al. 2012) to the ground state is a key contributor to the cooling of the cold ISM (see e.g. Lagache, Cousin & Chatzikos

* E-mail: s.balashev@gmail.com

2018). Since the collisional excitation coefficient, C_{12} , with atomic hydrogen is roughly $\propto T^{0.35}$ (at temperatures $T \gtrsim 100$ K) one can expect that the $C\text{II}^*$ collisional excitation ($\propto nC_{12} \propto T^{-0.65}P$, where n is a number density and P is a thermal pressure) will be more efficient in CNM than in WNM, that coexist at similar characteristic thermal pressures. To discuss this difference quantitatively, we need to properly describe the phase diagram of neutral ISM and its dependence on the external parameters in the medium.

3 THE PHASE DIAGRAM OF NEUTRAL ISM

We calculated the phase diagram for the neutral ISM assuming thermal balance as was done by Field et al. (1969), Wolfire et al. (1995), Wolfire et al. (2003), and Bialy & Sternberg (2019). We considered cooling by $\text{Ly}\alpha$ (see e.g. Spitzer 1978), $C\text{II}$, and O I fine-structure emission. The latter were calculated by considering excitation of fine-structure levels (see e.g. Klessen & Glover 2016) using collisional coefficients¹ from (Launay & Roueff 1977; Barinovs et al. 2005; Abrahamsson, Krems & Dalgarno 2007). We considered heating by photo electrons, cosmic rays, and turbulence dissipation. For the first two mechanisms, we used a standard description (see e.g. Bialy & Sternberg 2019) that depends on the electron fraction, obtained using similar calculations as in Balashev & Kosenko (2020). The turbulence dissipation heating is not well constrained in diffuse ISM due to its intermittent nature, i.e. variability of energy sources of the turbulence, and lacks direct observations. For simplicity, we assume an averaged $\Gamma_{\text{turb}} \sim \gamma_{\text{turb}}n$, where γ_{turb} has typical values of $\sim 10^{-27}$ erg s⁻¹ (see e.g. Elmegreen & Scalo 2004; Pan & Padoan 2009). This gives a comparable heating of the gas as provided by cosmic ray ionization rate (CRIR) of 10^{-16} s⁻¹.

An important point here is that the phase diagram of the neutral ISM depends on metallicity, as considered in details by several authors (Liszt 2002; Bialy & Sternberg 2019).² In Fig. 1, we show examples of phase diagrams at range of metallicities relevant for our study and calculated for CRIR = 10^{-16} s⁻¹, $\gamma_{\text{turb}} = 10^{-27}$ erg s⁻¹ and UV field $\chi = 1$ (in units of Draine field). The dependence on the metallicity is mostly seen as an increase of P_{min} (the minimum pressure for CNM) and P_{max} (the maximal pressure for WNM) with decreasing metallicity. This is due to the fine-structure line cooling that induces the transition between CNM and WNM (and therefore, determines P_{min} and P_{max}) scaling with metallicity, while the cosmic ray and turbulent heating – that dominate at low metallicities $Z \lesssim 0.1^3$ (Bialy & Sternberg 2019) – do not. The photoelectric heating, which is dominant heating at intermediate metallicities $Z \gtrsim 0.1$, is proportional to the dust-to-gas ratio (DTG) and hence scales with metallicity. However, observations indicate a non-linear dependence of DTG on Z in particular at low metallicities. For simplicity, in the following, we consider a single power-law dependence of DTG on Z with a slope $\alpha = 2.0$ for the whole range of metallicities (matching the observations from Rémy-Ruyer et al. 2014), and take into account its dispersion (see Section 6).

¹We assume that the main collisional partner in neutral ISM is atomic hydrogen. The presence of molecular hydrogen can slightly change the cooling, but this may become noticeable only for the dense medium, where the molecular fraction is high.

²We did not include the heating and cooling by molecular hydrogen, as considered by Bialy & Sternberg (2019), since it is not important for the range of metallicity and number density probed by $C\text{II}$, which is relevant for our study.

³Hereinafter, we note metallicity with respect to solar as Z .

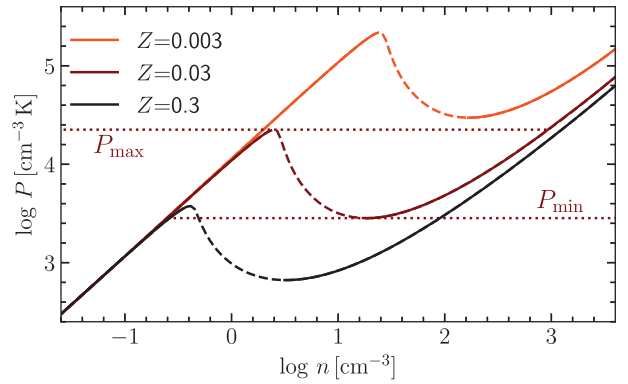


Figure 1. The dependence of phase diagram (pressure versus number density) of the neutral ISM on the metallicity. The black, brown, and red curves correspond to metallicities $Z = 0.3, 0.03,$ and $0.003,$ respectively. The dashed part of the curves is unstable. The other assumes parameters relevant for the calculation of the phase diagram are given in the text. Dotted horizontal lines indicate the maximal (resp. minimal) pressures where WNM (resp. CNM) can exist, calculated for the $Z = 0.03$ phase diagram.

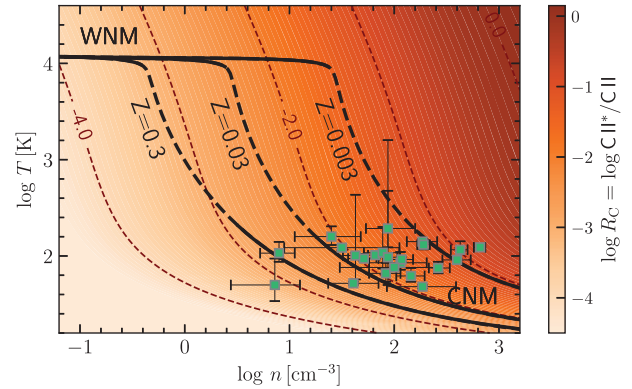


Figure 2. $C\text{II}^*/C\text{II}$ ratios at a function of number density and temperature. The dashed brown curves show the contours of the constant R_C . The black solid (and dashed) curves correspond to the stable (and unstable) branches of phase diagrams, calculated at the metallicities $Z = 0.3, 0.03, 0.003$ (indicated by text labels). Green circles indicate the measurements in H_2 -bearing components of DLAs (compiled mostly from Klimenko & Balashev 2020; Balashev et al. 2019, and references therein).

4 $C\text{II}^*/C\text{II}$ RATIO

Under typical ISM conditions, the $C\text{II}^*$ level is populated from the ground level by collisions (described by collision rate coefficient C_{12}) and depopulated by spontaneous decay (with the Einstein coefficient $A_{21} = 2.29 \times 10^{-6}$ s⁻¹). Hence the population ratio of $^2P_{3/2}^o$ and $^2P_{1/2}^o$ levels:

$$R_C = \frac{n(C\text{II}^*)}{n(C\text{II})} \approx \frac{C_{12}(T)n}{A_{21}}, \quad (1)$$

depends on the type of the collision partner (electron, atomic, or molecular hydrogen), the number density, n , and the temperature, T . In Fig. 2, we provide calculated R_C as a function of T and n assuming collisions with neutral hydrogen (Barinovs et al. 2005).⁴ We also overplot the phase diagrams calculated for different metallicities.

⁴Collision with electrons are sub-dominant as long as the ionization fraction is $\lesssim 10^{-2}$. We discuss the limiting case of IM separately in Section 7.

One can see that, following the phase diagram, R_C remains almost constant in the CNM (since C II fine-structure emission is the main coolant), but it steadily increases with number density (and pressure) in the WNM. Note also that, for a given metallicity, R_C remains much higher in the CNM than in the WNM, even at its maximal pressure. As metallicity decreases, the typical R_C increases for both the CNM and the WNM, owing to the increase of the characteristic number densities and temperatures. Since at $T \gtrsim 200$ K, the C II excitation is little sensitive to the temperature (see Fig. 2), it is important to emphasize that the observed R_C value can be used as a very useful probe of the number density in the WNM and lukewarm thermally unstable gas. In DLAs, where the temperature can be constrained (Noterdaeme et al. 2021), C II excitation will additionally provide a measurement of the thermal pressure.

5 OBSERVATIONS

The dependence of C II*/C II ratio on the metallicity can be investigated observationally in DLAs using measured column densities. Indeed, in DLAs $N(\text{C II}^*)$ can be directly constrained from its absorption spectrum (if the line is not significantly saturated), but it is not possible to directly measure the C II column density because of strong saturation of the absorption line. However, one can use the metallicity as a proxy for the abundance of carbon and constrain the C II*/C II ratio averaged over the velocity components of DLA as:

$$R_C \approx \frac{N(\text{C II}^*)}{N(\text{H I})(\text{C}/\text{H})_\odot \langle Z \rangle_{\text{DLA}}} \equiv \langle R_C \rangle_{\text{DLA}}, \quad (2)$$

where $\langle Z \rangle_{\text{DLA}}$ is the overall DLA metallicity, averaged over the velocity components⁵ and $(\text{C}/\text{H})_\odot$ is the solar abundance, taken from (Asplund et al. 2009).

In Fig. 3, we plot the measurements of C II*/C II ratio in DLAs as a function of metallicity,⁶ using a compilation of data from Wolfe et al. (2008), Dutta et al. (2014) and Telikova et al. (2021). We first note that there is a primary selection effect, making some regions of the diagram unavailable either due to weakness or saturation of C II* lines. These exclusion regions are illustrated by the greyed areas and limited by the dotted lines in Fig. 3. The latter correspond to $\log N(\text{C II}^*) = 12.5$ (detection limit) and 15 (saturation limit) represent the low and high end of $N(\text{C II}^*)$ distribution in the sample, respectively⁷ assuming the median $\log N(\text{H I})=21$. However, one can see that at a given metallicity the C II*/C II values are generally distributed into two groups of relatively *high* and *low* C II*/C II ratios (to highlight this, we overplot kernel density estimate of the sample). This separation is evident if we recall the fact that $R_C \sim l_c / \langle Z \rangle_{\text{DLA}}$, with evident bimodality in cooling rates, l_c , distribution (see also Wolfe et al. 2008, where the authors discussed metallicity distributions). To illustrate this, we highlight the points with $l_c < 10^{-27} \text{ erg s}^{-1}$ [considered by Wolfe et al. (2008) as ‘low’-cooling] by red colour. We also differentiate DLAs where molecular hydrogen is detected (green points) and found that these are located among the ‘high’ R_C population (see also Srianand et al. 2005). Indeed, the presence of molecular hydrogen is a clear indicator of the presence of CNM, which we confirm by measuring the kinetic

⁵We neglected depletion for carbon. Although the depletion is about 0.5 dex at solar metallicity, most DLAs in our sample have $\langle Z \rangle_{\text{DLA}} \lesssim 0.1$, where depletion is much less.

⁶The difference in the adopted solar abundances in the literature samples is within the metallicity uncertainties, so we do not take it into account here.

⁷This is only indicative since the exact range of reachable R_C for each system depends at least on the spectrum quality and the measured $\log N(\text{H I})$ (see equation 2). The latter spans about two dex in the considered sample.

temperature using the ortho-para ratio of H₂, and found ~ 100 K for all such DLAs (see Fig. 2). All this supports our hypothesis that the bimodality in the R_C - Z distribution originates from phase separation.

6 RESULTS

To further test whether CNM and WNM drive the bimodality of R_C - Z distribution, we estimated ranges of R_C in WNM and CNM as a function of metallicity using the calculation of the phase diagram, described in Section 3. For each metallicity on a grid (uniform in log scale) varying from 10^{-3} to 1, we generated a distribution of R_C in CNM and WNM by sampling the phase diagrams and characteristic pressures. Since DLAs likely probe the overall population of galaxies (Cen 2012), it certainly should have a dispersion in the physical conditions. We assumed lognormal distributions with 0.3 dex dispersion and mean of 1 (in Draine units) and $10^{-27} \text{ erg s}^{-1}$ for the intensity of the UV field and turbulence heating, respectively. We assumed a CRIR square-law dependence on UV with $\text{CRIR} = 10^{-16} \text{ s}^{-1}$ corresponding to Draine field (as constrained recently by Kosenko et al. 2021, and likely due to its association with star-formation). We also assume the same 0.3 dex dispersion for the DTG along its quadratic dependence on metallicity.

Then for each phase diagram, we estimated the ranges of R_C for CNM and WNM by sampling the pressure uniformly between P_{min} and P_{max} (see Fig. 1) estimated for each phase diagram. In Fig. 4, we show the obtained distribution of R_C for WNM and CNM as a function of metallicity constructed by such sampling. One can see that the phase separation of CNM and WNM explains R_C values measured in DLAs including the general metallicity dependence and the bimodality of R_C distribution at each metallicity. We note that the results are quite sensitive to the parameters of the UV, CRIR, and turbulence heating distributions, as well as to dependence DTG ratio on the metallicity (especially at the metallicity ranges $Z \gtrsim 0.1$) due to obvious dependence of the phase diagram on these parameters. In addition, the results – especially for WNM – depend on the sampling of pressures (this can be seen in Fig. 2, since R_C is very sensitive to n and hence P). We also note that the observed data points correspond to R_C averaged through the neutral gas in the DLA, while we consider only a single phase in our calculations. It is therefore hard to draw robust quantitative conclusions about the physical conditions in DLAs.

Notwithstanding, we can still qualitatively discuss the sampling of R_C - Z plane. Wolfe et al. (2008) proposed that the difference in the metallicity distribution of the ‘high-cool’ and ‘low-cool’ DLAs originates from different galaxy populations with different SFR regimes. However, as we showed above, the ‘high-cool’ and ‘low-cool’ sub-samples represent DLAs where C II* column density is predominantly associated with CNM and WNM, respectively. Since R_C is typically one order of magnitude higher in CNM than in WNM, then even if only a few CNM clouds are intercepted by the line of sight within a given DLA, these CNM clouds will contribute significantly to the total C II* (and also total H I) column densities, pushing the overall DLA value close to the pure CNM solution shown in Fig. 4. In that sense, the enhanced fraction of high-cool DLAs at $\log Z \gtrsim -1.3$ simply indicates a higher probability for the DLA line of sight to cross CNM gas. This can be explained by the increased number of components at high metallicity (see e.g. Ledoux et al. 2006) together with a higher probability for each of them to intersect CNM.⁸ This

⁸The minimal pressure required for the existence of CNM decreases with increasing metallicity (see Fig. 2), leading to a decrease of the characteristic number densities and hence an increase of the cross-section of such gas.

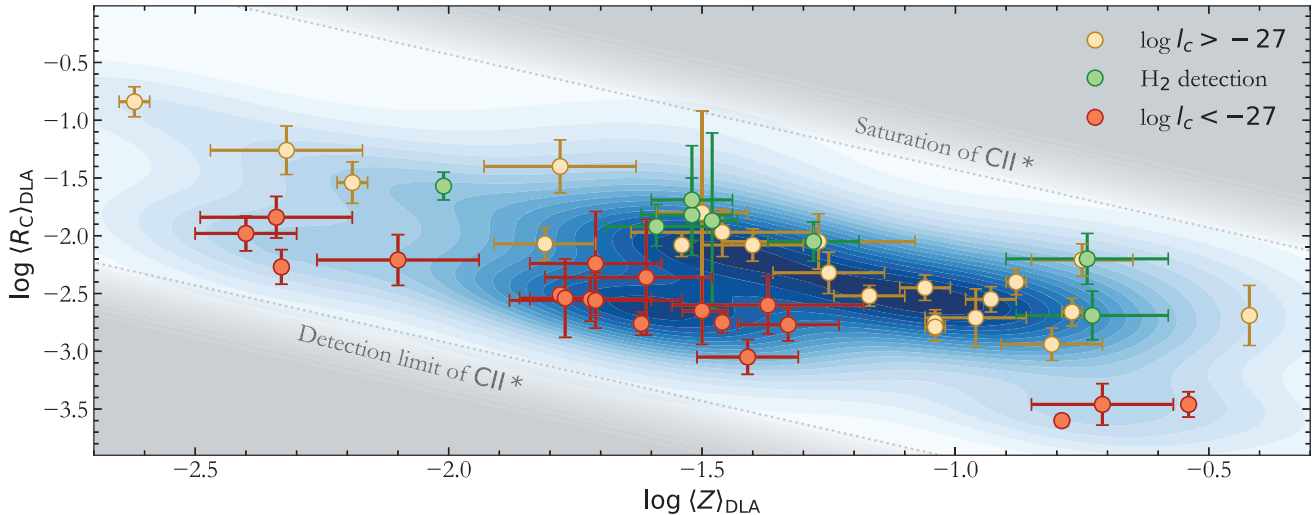


Figure 3. $\langle R_C \rangle_{\text{DLA}}$ as a function of the averaged metallicity observed in DLAs. The points with errorbars indicate the observed values towards QSO sightlines. The green points are DLA systems with H_2 detection. The red points correspond to the systems with low $C\text{II}^*$ cooling rate. The blue contours show the kernel density estimate of the sample. Grey areas correspond to the conditionally defined observational selection of $C\text{II}^*$: The bottom-left region represents the detection limit of $C\text{II}^*$, while the upper-right region corresponds to $C\text{II}^*$ saturation of lines, where measurements of $N(C\text{II}^*)$ are complicated (see the text for details).

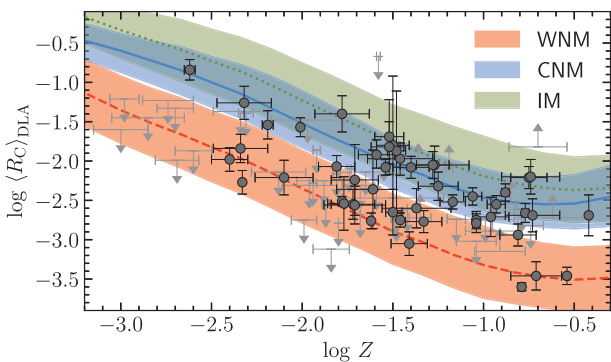


Figure 4. $C\text{II}^*/C\text{II}$ ratio as a function of the metallicity. The black points indicate the observed values towards QSO sightlines (the same as in Fig. 3, while the grey markers indicate upper and lower limits (taken from Wolfe et al. 2008; Dutta et al. 2014). The red, blue, and olive stripes show the ranges where located 68 per cent of the sampled distributions calculated for the warm neutral, cold neutral, and ionized medium (IM), respectively. The details of the calculation are provided in the text.

is confirmed by the higher H_2 incidence rate at higher metallicities (Petitjean et al. 2006; Noterdaeme et al. 2008; Balashev et al. 2019). Interestingly, while H_2 always probes CNM, it is detected only in about one fourth of the ‘high’ $\langle R_C \rangle_{\text{DLA}}$ (even though not all DLAs in the sample have a spectrum that covers the wavelength region where H_2 lines are located). Selecting high $\langle R_C \rangle_{\text{DLA}}$, could therefore, provide an interesting way to uncover a potentially large fraction of CNM that does not produce detectable H_2 absorption (as also noted by Krogager & Noterdaeme 2020). This fraction is however hard to quantify since our $C\text{II}^*$ sample is not fully representative to the whole DLA population. For example, the typical H_2 incidence rate in DLAs is quite low $\lesssim 10$ per cent (Noterdaeme et al. 2008; Balashev & Noterdaeme 2018), while it is found to be higher in this sample ($\gtrsim 15$ per cent), possibly owing to its skewed H I distribution (the H_2 detection rate is known to be much higher at the high end of the H I column density distribution, Noterdaeme et al. 2015; Balashev & Noterdaeme 2018; Ranjan et al. 2020).

7 IMPACT OF IONIZED MEDIUM

It is important to note that *high* $C\text{II}^*/C\text{II}$ ratios can also arise from IM, which was not taken into account in our model before. While studies of our Galaxy (e.g. Lehner, Wakker & Savage 2004) as well as modelling (e.g. Ramos Padilla et al. 2021) all indicate that a large fraction of $[C\text{II}] 158 \mu\text{m}$ emission can be associated with IM, there are doubts that the same holds for DLAs (e.g. based on the modelling of ion abundances Wolfe et al. 2004). However, in addition to neutral gas, the line of sight giving rise to DLAs may also cross ionized gas, owing to *in situ* production of ionizing photons in star-forming regions. Therefore, DLAs with total H I column densities sufficiently high for shielding from ionizing photons in a given individual cloud can still probe ionized phase as well. Indeed, absorption from metals in high-ionization stage is generally found associated with DLAs (see e.g. Fox et al. 2007). Regarding the ionized phase, the $C\text{II}^*$ fine-structure level can be significantly excited by collision with electrons.⁹ In Fig. 4, we plot the expected R_C in fully ionized gas assuming a temperature of $T_{\text{IM}} = 10^4 \text{ K}$ and using the same sampling of phase diagram and pressures as for CNM and WNM (see Section 6). One can see that if the fraction of IM along the line of sight is relatively high in DLAs (such IM is not detected in H I), then the integrated $C\text{II}^*/C\text{II}$ ratio can be much higher than the warm phase limit and mimic the presence of CNM. Unfortunately, while we have no constrain on the ionized fraction in DLAs, it is hard to argue how many of the observed $C\text{II}^*/C\text{II}$ ratios above the warm limit could originate from ionized gas.

8 CONCLUSIONS

We showed that the previously reported bimodality of observed $[C\text{II}]$ cooling rates (l_c) in DLAs is essentially the result of combining two effects: (i) The phase separation of the neutral ISM and (ii) the metallicity dependence of this phase splitting. The first results in a much higher $R_C = C\text{II}^*/C\text{II}$ ratio in CNM than in WNM owing to

⁹The electron excitation typically results in \sim order higher $C\text{II}^*/C\text{II}$ ratios than the collisions with atomic hydrogen for the same number density.

higher collisional excitation. The second maintains this bimodality as a function of Z , since $l_c \propto R_C/Z$. Importantly, the metallicity dependence is a consequence from the cooling of CNM being due to the fine-structure line, hence linearly scaling with Z , while the heating of the neutral gas becomes insensitive to the metallicity at low- Z , where it is dominated by cosmic rays (Bialy & Sternberg 2019). In the low metallicity regime, measuring the C II cooling rate (that is the main cooling only if DLA medium is predominantly associated with CNM), permits in fact to constrain the cosmic ray (and/or turbulence) heating – assuming thermal balance – but does not provide a direct measurement of the UV field. We note however that there may be a tight correlation between cosmic rays and UV field (Kosenko et al. 2021). If heating is dominated by cosmic rays, then using ‘high’- C II* DLAs (likely associated with CNM, where the cooling is due to C II* emission), we can write $\zeta_p = l_c E_{cr}^{-1}$, where $E_{cr} \approx 10^{-11}$ erg in neutral medium (e.g. Bialy & Sternberg 2019). The cosmic rays ionization rates in DLAs are then in the range $\approx 10^{-16} - 10^{-15} \text{ s}^{-1}$.

While measurements of R_C can be used to estimate the number density in the WNM or lukewarm gas, quantitative usage of the currently available measurements of R_C in DLAs is problematic due to non-trivial selection function, and unknown mixing of CNM and WNM along the line of sight. An additional impediment is the possible presence of a large amount of thermally unstable gas (see e.g. Kim & Ostriker 2017), that has R_C in between WNM and CNM. Finally, the unknown (and expected to be large) dispersion of the physical parameters (including DTG, CRIR, and turbulence heating) in DLAs also complicates the picture. Future studies of C II*/C II ratio should greatly benefit from detailed comparative component-by-component analysis of C II* absorption lines together with those of other species such as Si II or S II since C II is generally not accessible due to saturation of the line.

Finally, we note that the increase of the C II* excitation with decreasing metallicity is very important for a proper understanding of the [C II] $\lambda 158 \mu\text{m}$ emissivity function, in particular given the large efforts currently going on to detect galaxies using [C II] emission at low metallicities (see e.g. dwarf galaxy survey Madden et al. 2013) and at high redshifts ($\gtrsim 4$) (e.g. Maiolino et al. 2005; Wagg et al. 2012). Furthermore, at these redshifts, one should also take into account the fine-structure excitation by the CMB, which can alter the phase diagram and enhance [C II] $\lambda 158 \mu\text{m}$ line strength from WNM (see e.g. Liszt 2002).

ACKNOWLEDGEMENTS

We thank the anonymous referee for constructive comments and useful suggestions. This work was supported by RSF grant 18-12-00301 and by the French *Agence Nationale de la Recherche* under grant number 17-CE31-0011-01 (‘HIH2’).

DATA AVAILABILITY

The data underlying this article will be shared on reasonable request to the corresponding author.

REFERENCES

Abrahamsson E., Krens R. V., Dalgarno A., 2007, *ApJ*, 654, 1171
 Asplund M., Grevesse N., Sauval A. J., Scott P., 2009, *ARA&A*, 47, 481
 Balashev S. A., Kosenko D. N., 2020, *MNRAS*, 492, L45
 Balashev S. A., Noterdaeme P., 2018, *MNRAS*, 478, L7

Balashev S. A. et al., 2019, *MNRAS*, 490, 2668
 Barinova G., van Hemert M. C., Krens R., Dalgarno A., 2005, *ApJ*, 620, 537
 Bialy S., Sternberg A., 2019, *ApJ*, 881, 160
 Cen R., 2012, *ApJ*, 748, 121
 Draine B. T., 2011, *Physics of the Interstellar and Intergalactic Medium*. Princeton University Press, Princeton
 Dutta R., Srianand R., Rahmani H., Petitjean P., Noterdaeme P., Ledoux C., 2014, *MNRAS*, 440, 307
 Elmegreen B. G., Scalo J., 2004, *ARA&A*, 42, 211
 Field G. B., Goldsmith D. W., Habing H. J., 1969, *ApJ*, 155, L149
 Fox A. J., Ledoux C., Petitjean P., Srianand R., 2007, *A&A*, 473, 791
 Goldsmith P. F., Langer W. D., Pineda J. L., Velusamy T., 2012, *ApJS*, 203, 13
 Kanekar N. et al., 2014, *MNRAS*, 438, 2131
 Kim C.-G., Ostriker E. C., 2017, *ApJ*, 846, 133
 Klessen R. S., Glover S. C. O., 2016, *Saas-Fee Advanced Course*, 43, 85
 Klimenko V. V., Balashev S. A., 2020, *MNRAS*, 498, 1531
 Kosenko D. N., Balashev S. A., Noterdaeme P., Krogager J. K., Srianand R., Ledoux C., 2021, *MNRAS*, 505, 3810
 Krogager J.-K., Noterdaeme P., 2020, *A&A*, 644, L6
 Lagache G., Cousin M., Chatzikos M., 2018, *A&A*, 609, A130
 Launay J. M., Roueff E., 1977, *A&A*, 56, 289
 Ledoux C., Petitjean P., Fynbo J. P. U., Møller P., Srianand R., 2006, *A&A*, 457, 71
 Lehner N., Wakker B. P., Savage B. D., 2004, *ApJ*, 615, 767
 Liszt H., 2002, *A&A*, 389, 393
 Madden S. C. et al., 2013, *PASP*, 125, 600
 Maiolino R. et al., 2005, *A&A*, 440, L51
 Neeleman M., Prochaska J. X., Wolfe A. M., 2015, *ApJ*, 800, 7
 Noterdaeme P., Ledoux C., Petitjean P., Srianand R., 2008, *A&A*, 481, 327
 Noterdaeme P., Srianand R., Rahmani H., Petitjean P., Pâris I., Ledoux C., Gupta N., López S., 2015, *A&A*, 577, A24
 Noterdaeme P. et al., 2021, *A&A*, 651, A78
 Pan L., Padoan P., 2009, *ApJ*, 692, 594
 Petitjean P., Ledoux C., Noterdaeme P., Srianand R., 2006, *A&A*, 456, L9
 Pineda J. L., Langer W. D., Velusamy T., Goldsmith P. F., 2013, *A&A*, 554, A103
 Pottasch S. R., Wesselius P. R., van Duinen R. J., 1979, *A&A*, 74, L15
 Ramos Padilla A. F., Wang L., Ploeckinger S., van der Tak F. F. S., Trager S. C., 2021, *A&A*, 645, A133
 Ranjan A., Noterdaeme P., Krogager J. K., Petitjean P., Srianand R., Balashev S. A., Gupta N., Ledoux C., 2020, *A&A*, 633, A125
 Rémy-Ruyer A. et al., 2014, *A&A*, 563, A31
 Roy N., Frank S., Carilli C. L., Mathur S., Menten K. M., Wolfe A. M., 2017, *ApJ*, 834, 171
 Spitzer L., 1978, *Physical Processes in the Interstellar Medium*. WILEY-VCH Verlag GmbH & Co. KGaA, Weinheim, doi:10.1002/9783527617722
 Srianand R., Petitjean P., Ledoux C., Ferland G., Shaw G., 2005, *MNRAS*, 362, 549
 Telikova K. N., Balashev S. A., Noterdaeme P., Krogager J.-K., Ranjan A., 2021, *MNRAS*, submitted
 Wagg J. et al., 2012, *ApJ*, 752, L30
 Wolfe A. M., Prochaska J. X., Gawiser E., 2003, *ApJ*, 593, 215
 Wolfe A. M., Howk J. C., Gawiser E., Prochaska J. X., Lopez S., 2004, *ApJ*, 615, 625
 Wolfe A. M., Gawiser E., Prochaska J. X., 2005, *ARA&A*, 43, 861
 Wolfe A. M., Prochaska J. X., Jorgenson R. A., Rafelski M., 2008, *ApJ*, 681, 881
 Wolfire M. G., Hollenbach D., McKee C. F., Tielens A. G. G. M., Bakes E. L. O., 1995, *ApJ*, 443, 152
 Wolfire M. G., McKee C. F., Hollenbach D., Tielens A. G. G. M., 2003, *ApJ*, 587, 278

This paper has been typeset from a $\text{\TeX}/\text{\LaTeX}$ file prepared by the author.